



Article

Improving Fabrication and Performance of Additively Manufactured RF Cavities by Employing Co-Printed Support Structures and Their Subsequent Removal

Michael Mayerhofer ^{1,*}, Stefan Brenner ², Michael Doppler ³, Luis Catarino ⁴, Stefanie Girst ¹, Vesna Nedeljkovic-Groha ² and Günther Dollinger ¹

¹ Institute for Applied Physics and Measurement Technology (LRT2), Universität der Bundeswehr München, Werner-Heisenberg-Weg 39, 85577 Neubiberg, Germany

² Institute for Design and Production Engineering, Universität der Bundeswehr München, Werner-Heisenberg-Weg 39, 85577 Neubiberg, Germany

³ RENA Technologies Austria GmbH, Samuel-Morse-Straße 1, 2700 Wiener Neustadt, Austria

⁴ FKM Sintertechnik GmbH, Zum Musbach 6, 35216 Biedenkopf, Germany

* Correspondence: michael.mayerhofer@unibw.de

Abstract: The enormous potential of additive manufacturing (AM), particularly laser powder bed fusion (L-PBF), to produce radiofrequency cavities (cavities) has already been demonstrated. However, the required geometrical accuracy for GHz TM_{010} cavities is currently only achieved by (a) avoiding downskin angles $< 40^\circ$, which in turn leads to a cavity geometry with reduced performance, or (b) co-printed support structures, which are difficult to remove for small GHz cavities. We have developed an L-PBF-based manufacturing routine to overcome this limitation. To enable arbitrary geometries, co-printed support structures are used that are designed in such a way that they can be removed after printing by electrochemical post-processing, which simultaneously reduces the surface roughness and thus maximizes the quality factor Q_0 . The manufacturing approach is evaluated on two TM_{010} single cavities printed entirely from high-purity copper. Both cavities achieve the desired resonance frequency and a Q_0 of approximately 8300.

Keywords: additive manufacturing; cavity; linac; 3D printing; pure copper; LPBF; SLM; selective laser melting; gradient model; RF losses; surface roughness model; electrochemical post-processing; support structures



Citation: Mayerhofer, M.; Brenner, S.; Doppler, M.; Catarino, L.; Girst, S.; Nedeljkovic-Groha, V.; Dollinger, G. Improving Fabrication and Performance of Additively Manufactured RF Cavities by Employing Co-Printed Support Structures and Their Subsequent Removal. *Instruments* **2024**, *8*, 18. <https://doi.org/10.3390/instruments8010018>

Academic Editor: Antonio Ereditato

Received: 16 December 2023

Revised: 21 February 2024

Accepted: 23 February 2024

Published: 1 March 2024



Copyright: © 2024 by the authors. Licensee MDPI, Basel, Switzerland. This article is an open access article distributed under the terms and conditions of the Creative Commons Attribution (CC BY) license (<https://creativecommons.org/licenses/by/4.0/>).

1. Introduction

Around the world, 35,000 particle accelerators are used to propel charged particles (e.g., electrons, protons) to high energies [1,2]. They are indispensable for accelerator-based research, medical applications such as radiotherapy for cancer, or industrial applications like X-ray inspection [1,3–6]. The fundamental components of most linear particle accelerator (Linacs) are radiofrequency (RF) cavities made of conductive material like copper or niobium. To accelerate charged particles, a sinusoidal alternating signal (RF signal) with a frequency corresponding to the resonance frequency f_R of the cavity is coupled into the cavity, resulting in a high-gradient electromagnetic (EM) field [1].

In conventional manufacturing, cavities are manufactured from numerous individual parts due to their complex internal geometry, essential for generating high E-field strengths or cooling. The individual parts must be joined through processes such as brazing, electron beam welding or similar methods to achieve vacuum tightness and maximum electrical conductivity. This multi-stage manufacturing process limits the freedom in design and thus new innovative cavity concepts required for linacs with, for example, lower energy consumption or longer operating times [2,7–9]. Moreover, the conventional manufacturing process is responsible for over 35% of the investment costs for Linacs [10–12], which can be significantly reduced through additive manufacturing.

In comparison to traditional manufacturing processes, additive manufacturing (AM, 3D printing) presents numerous advantages. The capability to fabricate intricate geometries in a single piece allows for performance optimization of components, eliminating the need for expensive tooling and minimizing material consumption. Additionally, AM enables rapid prototyping and decentralized production which significantly expediting the product development process [13,14].

The latest research results obtained on various cavity prototypes indicate that additive manufacturing has the potential to overcome the limitations of the conventional manufacturing process [15–23]. For example, the laser powder bed fusion process (L-PBF, also known as PBF-LB) [13,24,25] makes it possible to manufacture cavities made of high-purity copper, including the internal geometry, in one piece [22,23]. Thereby, geometrical accuracy sufficient for resonance frequencies $f_R < 4$ GHz and quality factors (Q_0) comparable to conventionally manufactured structures is achieved [22,23]. As depicted in Figure 1, a limitation of L-PBF is the necessity for support structures to prevent overhangs, commonly referred to as downskin sections, from deforming as they are printed onto the loose powder bed. A downskin surface with an angle of approximately $\alpha > 40^\circ$ between the building platform (black) and the downskin surface allows for high quality (Figure 1a). Without a support structure, a downskin angle $\alpha < 40^\circ$ results in the irregular and rough production of the desired topology (Figure 1b).

The removal of support structures from centimeter-sized GHz cavities has always been considered a major challenge. Therefore, a design guide for self-supporting cavity geometries with the condition $\alpha > 40^\circ$ was developed [26]. However, this condition results in a reduction in Q_0 by up to 18% in the case of TM_{010} cavities and thus limits the potential of AM for cavity manufacturing [27].

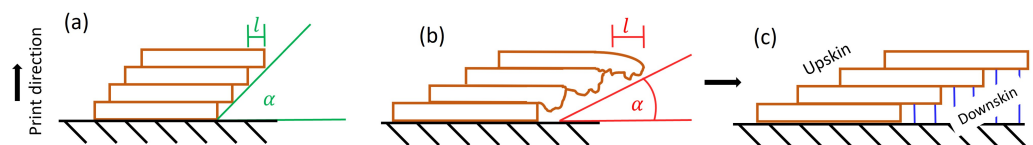


Figure 1. Representation of four printed layers (brown) creating an overhang with an angle α relative to the building platform (black). (a) Optimal print quality is achievable with a larger α . (b) Layer deformation becomes more pronounced as α decreases. (c) The introduction of a support structure (blue) is necessary to maintain print quality when $\alpha < 40^\circ$. The graphic was adapted from [27].

In this article, we present a manufacturing routine based on L-PBF and an electrochemical post-processing method that allows the realization of arbitrary cavity geometries with the assistance of co-printed support structures. However, the co-printed support structures are designed in such a way that subsequent removal is possible in the cavity with the electrochemical post-processing method (Hirtisation (R)) [28]. This approach is demonstrated using two identical TM_{010} 3 GHz single-cell cavities (SC), as commonly employed in, e.g., Drift Tube Linac (DTL) or Coupled Cavity Linac (CCL) structures [1]. Both SCs were manufactured from high-purity copper. Their performance is evaluated through RF measurements. Subsequently, the measurements are compared with CST Microwave Studio (R) (CST) simulations [29].

2. Materials and Methods

2.1. Cavity Design and Electromagnetic (EM) Simulation

The cavity design is based on a typical rudimentary geometry of a single TM_{010} accelerator cell, as specified, for example, in the Poisson Superfish cavity design software [30] (see Figure 2a). All electromagnetic (EM) simulations for this work were conducted using the Eigenmode solver or frequency domain solver of the 3D EM analysis tool CST Microwave Studio (R).

We aimed to achieve an f_R of 2997.9 MHz for the SCs, which corresponds to the operating frequency of "3 GHz" Linac systems for medical radiotherapy [31,32]. However,

in the case of the SCs, the goal is to attain this f_R at normal pressure to simplify the RF measurements. f_R is proportional to $\frac{1}{\sqrt{LC}}$, where L corresponds to the inductance and C to the capacitance of a cavity. The capacitance C is primarily influenced by the nose cone's distance and shape, while the inductance L is mainly determined by the cavity's diameter. Changes in L or C depend on relative alterations in the geometric dimensions. Consequently, an increase in f_R is anticipated, given that the greatest impact is expected from the relative change in the geometric parameter g . Previous prototypes manufactured with the same post-processing method show a frequency shift in dependence on the material removal (MR) (by Hirtisation (R)) of approximately $+0.18 \frac{\text{MHz}}{\mu\text{m}}$ [22]. To provide enough material for the removal of the support structure and the reduction of the surface roughness, a f_R reduced by 60 MHz to 2937.9 MHz was planned for printing.

The table in Figure 2b displays the geometry parameters of the SCs that CST simulated with $f_R = 2937.92$ MHz. The parameters largely correspond to the single cavities used in 3 GHz side-coupled cavity Linacs (SCCL) as part of Linac-based proton therapy systems [31,32]. In terms of electromagnetic properties, it can therefore be assumed that the SC geometry is optimized. The cavity length L was set to 23 mm, corresponding to proton energy of about 26 MeV in a 2π -mode Linac ($\beta_{proton} \approx 0.23$). The printing direction was chosen perpendicular to the beam axis.

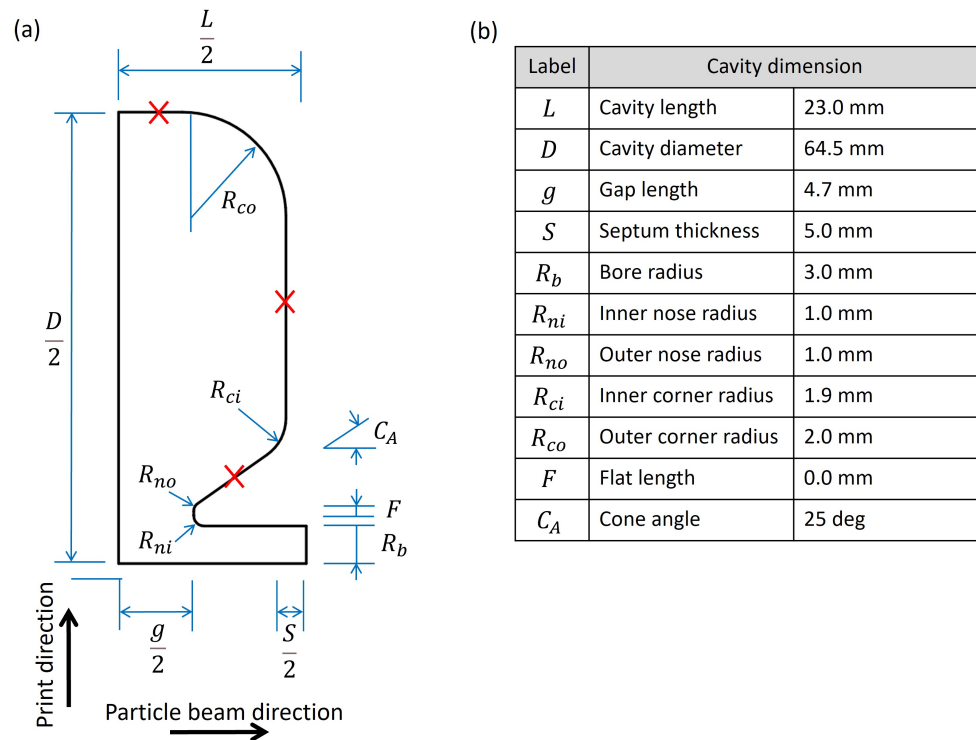


Figure 2. (a) First quadrant of the longitudinal section through a conventional TM_{010} single cavity. The red crosses mark the locations of the surface roughness measurements. (b) Relevant geometric parameters of the printed SC.

2.2. Additive Manufacturing

The SCs were manufactured using L-PBF. An EOS AMCM M290 with a maximum laser power of 1 kW, located at FKM Sintertechnik GmbH, was utilized. The dimensions of the build chamber are $250 \times 250 \times 310$ mm. The raw material used is pure copper (CuCP) from the company EOS GmbH. The chemical composition of the powder is Cu (99.95%), O (0.04%) and a residue of various elements (0.01%). The general particle size distribution corresponds to $D_{10} = 19.4 \mu\text{m}$, $D_{50} = 35.2 \mu\text{m}$ and $D_{90} = 48.5 \mu\text{m}$ [33]. The printed structures have relative densities of over 99.5%. Thus, electrical conductivity between 97.4 and 100.2% (IACS) can be achieved [34].

To ensure the necessary geometric accuracy for a f_R of 3 GHz, the downskin surfaces were supported by co-printed structures. Figure 3 shows the support structure designed for this purpose (red and yellow) in an SC (grey). A block support design was employed to provide broad support for the downskin areas. A wide mesh (hatching distance 3 mm) and a special perforation pattern were utilized to achieve the best possible process media flow during post-processing. To minimize contact points with the cavity surface, the individual struts of the block support were gradually thinned towards the surface. The exact structure of the support is a trade secret of FKM Sintertechnik GmbH and will therefore not be disclosed in this paper.

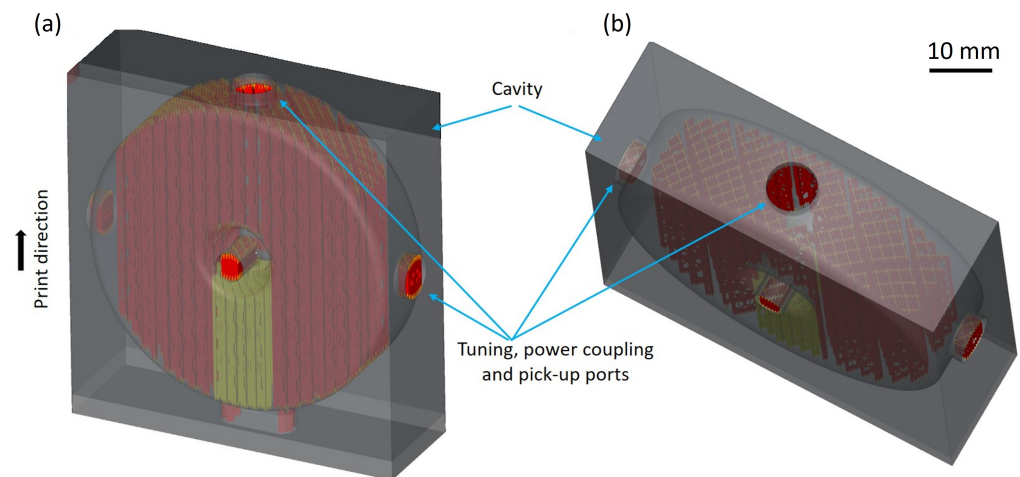


Figure 3. Front view (a) and top view (b) of the SC (grey) with co-printed support structure (red and yellow).

2.3. Post-Processing Procedure

The post-processing is based on the process of Hirtisation (R) developed by RENA GmbH Hirtisation. Hirtisation (R) is a combination of different chemical/electrochemical processes. The aim of the process is to remove sintered-on particles as well as support structures and to smooth the component surface by removing the protruding parts of a surface profile faster than recesses. In contrast to processes like chemical mechanical planarization (CMP) or those using an abrasive fluidic medium, there are no mechanical processes included. The processing time depends on the component characteristics (alloy, heat treatment, printing parameters, etc.) and current process medium activity. The required material removal is achieved by measuring the material removal rate for the particular parts during the process. Material removal was measured with a micrometer caliper at the shortest dimension of the outer cuboid structure near the corners given the one-sided material removal by simple division by two. Positive results with regard to surface roughness and Q_0 have already been achieved with this method on earlier prototypes [23]. The post-processing is carried out in two steps (PPS 1 and PPS 2).

PPS 1: Co-printed support structures are completely dissolved in a first Hirtisation (R) step.

PPS 2: After step 1, f_R is determined, allowing the calculation of how much material removal (MR) is still required to reach 2997.9 MHz. This MR is then realized by a second Hirtisation (R) step. In addition, PPS 2 further reduces the surface roughness and thus increases Q_0 .

The process media Cu-Auxilex and Cu-Delevatex are used in both steps, with Cu-Delevatex being used for the last 10 μm of fine adjustment. Like the Hirtisation process, Cu-Auxilex and Cu-Delevatex were also developed by RENA Technologies Austria GmbH [28].

2.4. RF Measurements

In this study, we evaluate the resonant frequency f_R and the unloaded quality factor Q_0 of the cavities. Achieving the planned f_R is crucial for stable cavity operation and to attain the highest possible particle acceleration. Even in conventional manufacturing, deviations from the planned geometry and thus the planned f_R cannot be avoided. For successful frequency tuning after production, however, Δf should be minimized. With conventional manufacturing methods, a Δf of approximately 2 MHz is achieved for diamond-tooled 3 GHz TM_{010} cavities [35]. The unloaded quality factor $Q_0 = \frac{\omega W}{P}$ measures the cavity's capacity to store energy and consequently reflects the attainable electric field strength. Here, ω is the angular frequency of the RF signal, W represents the stored energy and P denotes the power loss.

f_R and Q_0 are determined using a Siglent SNA5012A vector network analyzer (VNA) and a coupling loop probe (CLP) via a reflection measurement (S11). The VNA was calibrated to the end of the CLP. All measurements refer to the TM_{010} mode of the respective SCs.

2.5. Evaluation of Inner Geometry and Surface Roughness

To evaluate the inner geometry, the SCs are cut in half and examined using a Keyence VR-5000 3D wide-area 3D measurement system (Keyence, Osaka, Japan). This system utilizes the structured light method with $12\times$ magnification and features an automatic stage. A false color plot is generated by comparing the resulting 3D data to the CAD data. The measurement accuracy is limited to $\pm 4 \mu\text{m}$ with image stitching.

As in our previous work, we utilize the parameter $S_{\lambda q}$ (adapted from the area root-mean-square average S_q , ISO 25178) to describe the surface roughness [27]. The measured surface profile is recorded using a Keyence VK-X3000 laser scanning microscope. The feasible working distance to the cavity surface allows the use of the $50\times$ objective at normal surfaces ($\alpha = 90^\circ$) and the use of the $20\times$ objective in the version with an extra-long working distance at the downskin and upskin surfaces. Subsequently, the surface profiles undergo post-processing through the Keyence software functions *Noise removal* (set to "High") and *missing data removal*. Additionally, a form correction operator (F-Operator) with a wavelength of $\lambda_f = 130 \mu\text{m}$ is applied. Surface variations characterized by a wavelength $\lambda \gg \delta$ appear to have only a minor impact on the surface conductivity [23,27]; therefore, another high-pass filter (λ_c filter) is applied. Thereby, λ_c is defined as the copper powder size D_{50} , and $\lambda_c = D_{50} = 35.2 \mu\text{m}$.

$S_{\lambda q}$ is determined at six locations on the inner cavity surface. Three of these locations are shown in Figure 2 by a red cross in the first quadrant of the cell longitudinal section. The other three were measured at the corresponding locations in the third quadrant of the cell. The measuring locations are numbered in ascending order in the printing direction. An area of around 1 mm^2 was evaluated at every location.

3. Results

Two cavities (SC 1 and SC 2) were manufactured using the methods described in Section 2. To completely remove the support structure, material removal (MR) of $130 \mu\text{m}$ was required in PPS 1. In PPS 2, MR of $140 \mu\text{m}$ was processed to further increase Q_0 and reach the desired f_R of 2997.9 MHz (compare Sections 3.1 and 3.2). Figure 4 shows the additively manufactured cavities SC 1 and SC 2 after PPS 2.

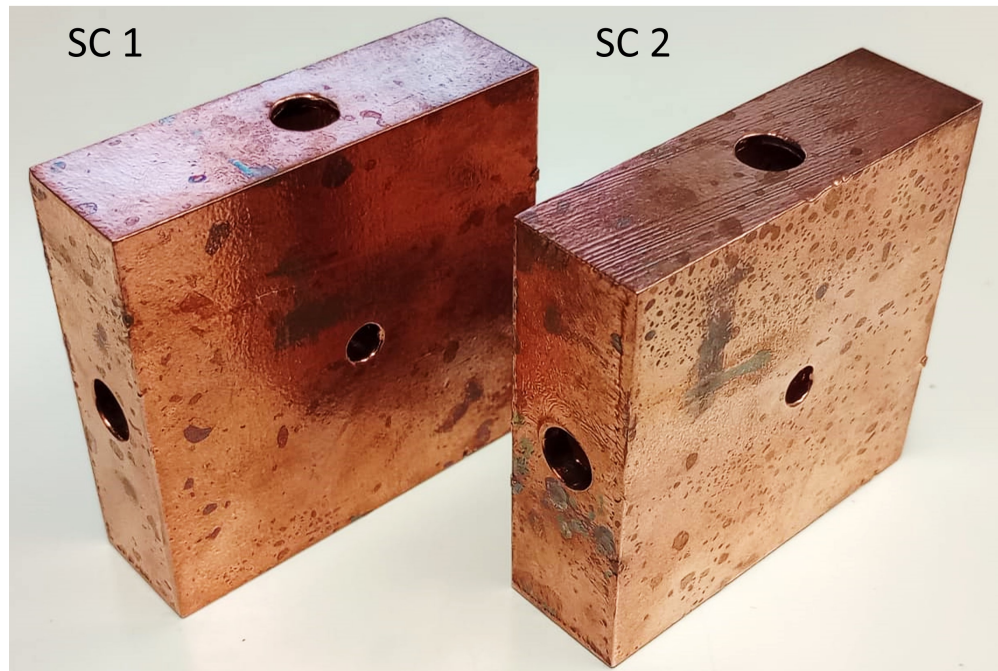


Figure 4. SC 1 and SC 2 after PPS 2.

3.1. Resonance Frequency f_R and Tuning Process

Due to the printed support structure, f_R was determined after each of the two post-processing steps, PPS 1 and PPS 2. Table 1 shows the measured f_R of the two SCs after the respective post-processing step. The averaged resonance frequency \bar{f}_R of the two structures after MR of $130\ \mu\text{m}$ by PPS 1 corresponds to $2970.4\ \text{MHz}$. The f_R of SC 1 and SC 2 deviate from each other by $1.2\ \text{MHz}$. Compared to the simulated $f_R = 2937.9\ \text{MHz}$ of the printed SCs, this corresponds to a material removal rate $\frac{\Delta f}{MR}$ of approximately $0.26\ \frac{\text{MHz}}{\mu\text{m}}$.

The iterative tuning process ended after PPS 2 with the further removal of $MR = 140\ \mu\text{m}$. After PPS 2, \bar{f}_R corresponds to $2997.3\ \text{MHz}$ and thus deviates only by $0.6\ \text{MHz}$ or $0.02\ \%$ from the planned f_R . With respect to f_R after PPS 1, this corresponds to a material removal rate $\frac{\Delta f}{MR}$ of approximately $0.20\ \frac{\text{MHz}}{\mu\text{m}}$. Considered independently, SC 1 and SC 2 deviate from the planned f_R by $0.2\ \text{MHz}$ and $1.0\ \text{MHz}$, respectively.

Table 1. f_R of SC 1 and 2, after PPS 1 and PPS 2.

	f_R —SC 1	f_R —SC 2
After PPS 1	$(2972.0 \pm 0.2)\ \text{MHz}$	$(2970.8 \pm 0.2)\ \text{MHz}$
After PPS 2	$(2997.7 \pm 0.2)\ \text{MHz}$	$(2996.9 \pm 0.2)\ \text{MHz}$

3.2. Unloaded Quality Factor Q_0

As with f_R , Q_0 was determined after the PPS 1 and PPS 2 treatments. Table 2 shows the measured Q_0 of the two SCs after the respective post-processing steps. After PPS 1, the SCs achieved an average quality factor \bar{Q}_0 of 5305 . The Q_0 of the two SCs are identical within the limits of the measurement uncertainties. \bar{Q}_0 reaches 8285 after PPS 2. The Q_0 simulated by CST corresponds to 9170 ± 50 . For the simulation, MR of $270\ \mu\text{m}$ (PPS 1 and PPS 2) was taken into account for the SC geometry. Therefore, after PPS 2, Q_0 corresponds to approximately 90% of the simulated Q_0 . The Q_0 values of the individual SCs differ slightly from each other, by approximately 3% .

Table 2. Q_0 of SC 1 and 2, after PPS 1 and PPS 2.

	Q_0 —SC 1	Q_0 —SC 2
After PPS 1	5340 ± 100	5270 ± 100
After PPS 2	8410 ± 100	8160 ± 100

3.3. Inner Geometry and Surface Roughness

Figure 5 displays the color-coded geometric difference z between the planned SC geometry, reduced by $270 \mu\text{m}$ (CAD data), and the measured surface data for the two halves (a and b) of the two SCs. Positive and negative values indicate areas with higher or lower material thickness than aimed for, respectively. A maximum deviation in the order of 0.25 mm is observed at the nose cone. Moreover, all SC halves exhibit waviness where the crests (the troughs) run roughly parallel to the printing direction. This is exemplarily shown for SC 2—a. Additionally, it is noticeable that an above-average amount of material was removed above and below the nose cones.

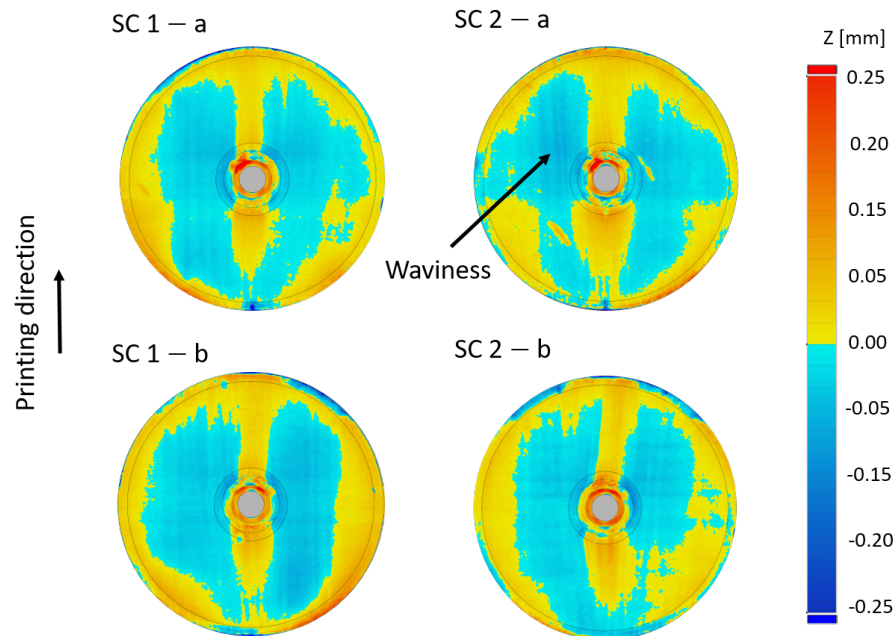


Figure 5. Difference between measured surface and CAD data Z of the individual SCs after PPS 2.

Table 3 presents the measured surface roughness $S_{\lambda q}$ at the different measurement locations 1–6 of SC 1 and SC 2 after PPS 2 (see Section 2.5). The upskin surfaces of the cavities (locations 1 and 4) exhibit an average $S_{\lambda q}$ of approximately $0.46 \mu\text{m}$. The surfaces parallel to the printing direction (locations 2 and 5) show an average $S_{\lambda q}$ of around $0.30 \mu\text{m}$. The downskin surfaces (locations 3 and 6) show an average $S_{\lambda q}$ of approximately $0.54 \mu\text{m}$. The mean value $\bar{S}_{\lambda q}$ of all $S_{\lambda q}$ amounts to $(0.43 \pm 0.1) \mu\text{m}$.

Table 3. $S_{\lambda q}$ of SC 1 and SC 2 after PPS 2 at the defined measurement locations (see Figure 2 and compare Section 2.5).

Measurement Location	$S_{\lambda q}$ —SC 1	$S_{\lambda q}$ —SC 2	Orientation
1	$0.49 \mu\text{m}$	$0.44 \mu\text{m}$	upskin
2	$0.31 \mu\text{m}$	$0.36 \mu\text{m}$	parallel
3	$0.57 \mu\text{m}$	$0.50 \mu\text{m}$	downskin
4	$0.46 \mu\text{m}$	$0.45 \mu\text{m}$	upskin
5	$0.28 \mu\text{m}$	$0.26 \mu\text{m}$	parallel
6	$0.58 \mu\text{m}$	$0.50 \mu\text{m}$	downskin

4. Discussion

4.1. Inner Geometry

The measurement uncertainty of the Keyence VR-5000 is $\pm 4 \mu\text{m}$. Additionally, the uncertainty in material removal by Hirtisation (R) is approximately $\pm 10 \mu\text{m}$. However, the CAD file used precisely corresponds to an SC geometry with removal of $MR = 270 \mu\text{m}$. From a geometric perspective, a gap length g deviation of about $1 \mu\text{m}$ corresponds to an Δf_R of about 0.2 MHz. The Z uncertainty thus results in uncertainty of approximately $\pm 2 \text{MHz}$ for f_R . Nevertheless, Figure 5 allows for an evaluation of the general shape and quality of the manufacturing process.

The waviness on the inner cavity surface can likely be explained as follows: during post-processing, gas bubbles form due to the chemical reaction, and they can move along preferred paths, resulting in differences in material removal, which manifests as waviness (see Figure 5). The general geometrical asymmetry (see Figure 5) is probably attributed to maintaining the geometry orientation in the process medium throughout the process. Therefore, the asymmetry is likely influenced by the flow direction of the process medium. For low-gradient cavities with E-fields in the range of a few $\frac{MV}{m}$, the geometry deviation resulting from the waviness and asymmetry might be tolerable as long as f_R is reached (see Section 4.2). However, in high-gradient operation, typical for most Linacs, this could lead to EM field peaks and, consequently, to breakdown events.

4.2. Resonant Frequency f_R and Tuning Process

The deviation Δf_R of the individual f_R of SC 1 and SC 2, as well as their average \bar{f}_R , from the planned f_R of 2997.9 MHz is always below 1.0 MHz. This is fully comparable to the Δf_R achieved in conventional manufacturing approaches. Such deviations can be easily corrected by standard frequency tuning devices (e.g., tuning rods), which are typically designed for 3 GHz Linacs to correct a Δf_R of a few MHz [35]. Therefore, our approach enables the manufacturing of TM_{010} cavities with $f_R < 3 \text{GHz}$ in sufficiently high geometrical accuracy to reach the desired f_R . Nevertheless, future studies should investigate in detail the influence of plastic deformation as the preferred tuning method for high-gradient applications on additively manufactured cavities.

4.3. Unloaded Quality Factor Q_0 and Surface Roughness

The unloaded quality factor \bar{Q}_0 was increased by PPS 2 to approximately 90% of the simulated Q_0 . The simulated Q_0 corresponds to the best possible value for a flat ($S_{q\lambda} = 0$) and annealed ($\sigma = 5.8 \cdot 10^7 \frac{\text{S}}{\text{m}}$, 100 % IACS) copper surface. As previously described by us in [27], the gradient model developed by Gold et al. [36] can be used to simulate the influence of surface roughness on the surface impedance and thus Q_0 with the help of the CST frequency domain solver. For the simulation, the surface roughness is assumed to be uniform over the entire cavity geometry. The assumed surface roughness $\bar{S}_{q\lambda}$ is obtained by averaging the measured surface roughness values from Table 3 to $0.43 \mu\text{m}$. This assumption was made because the surface roughness values of the upskin, downskin and normal surfaces are quite similar (standard deviation: $\sigma_{\bar{S}_{q\lambda}} = 0.1 \mu\text{m}$). However, since the areas of the different surfaces (upskin, downskin and normal) are not the same size, and the current densities on the cavity surface vary, the CST simulation's accuracy could be increased by assigning the individual cavity sections their exact surface roughness. However, since the surface roughness varies depending on α , the printing orientation, etc., and the geometry consists of transitions between the upper, lower and normal surfaces (e.g., nose cone), the exact assignment of the surface roughness requires considerable effort in terms of measurements and simulation.

The quality factor $Q_{\lambda 0}$ corrected with $\bar{S}_{q\lambda}$ is 8300 ± 50 , which corresponds to $\bar{Q}_0 = 8285$ measured after PPS 2, considering measurement uncertainties. This implies that the gradient model is valid for the single cavities presented here and that the single cavities have the same surface conductivity as a perfect, conventionally manufactured cavity with the same roughness. A comparison with the SCs presented in a previous study [27] reveals

an increase in $Q_{\lambda 0}$ by 10–20%, indicating progress in the manufacturing process. However, it should be noted that the SCs presented in [27] were printed on an L-PBF system based on green laser technology, not red laser technology. Different L-PBF systems vary in terms of the process parameters, the atmosphere in the build space, etc. Therefore, the comparison between the SCs may not be entirely valid, as different process parameters lead to distinct material properties, such as grain sizes or impurity concentrations. Although the method of post-processing was not changed between [27] and the present work, the success of post-processing and, consequently, the increase in surface conductivity may vary due to the different material properties. These results motivate further research, including a comparison of different L-PBF technologies for the manufacturing of cavities.

5. Conclusions

A novel additive manufacturing approach for high-frequency cavities was developed employing co-printed support structures to provide increased design freedom in laser powder bed fusion (L-PBF) for the production of TM_{010} cavities. The study demonstrated that electrochemical post-processing methods (Hirtisation (R)) can successfully remove co-printed support structures, even from small GHz cavities. The same post-processing procedure also serves to tune the cavities to the desired resonance frequency (f_R). Simultaneously, the quality factor (Q_0) of the cavities is enhanced by reducing the surface roughness. Consequently, the studies presented here show, for the first time, a GHz cavity printed entirely from pure copper that achieves both the simulated quality factor and resonant frequency simultaneously. Our manufacturing approach enables the production of small TM_{010} cavities with an optimal geometry from an electromagnetic field perspective using L-PBF. It is reasonable to assume that the cavities manufactured in this way are at least as efficient as conventionally manufactured structures in terms of particle acceleration.

However, before AM cavities are used in Linac systems, their performance under high input power and, consequently, their breakdown resistance at high E-field strengths ($E_z > 40$ MeV) must be evaluated. A test bench based on a magnetron amplifier is currently being developed for these high-gradient tests.

Author Contributions: Conceptualization, M.M. and G.D.; Methodology, M.M., S.B., M.D. and L.C.; Software, M.M., S.B. and L.C.; Validation, M.M. and G.D.; Formal analysis, M.M., S.B. and S.G.; Investigation, M.M.; Resources, G.D., S.B., M.D., L.C. and V.N.-G.; Data curation, M.M.; Writing—original draft preparation, M.M. and G.D.; Writing—review and editing, M.M., S.B., M.D., L.C., S.G., V.N.-G. and G.D.; Visualization, M.M. and S.B.; Supervision, G.D.; Project administration, M.M.; Funding acquisition, G.D. All authors have read and agreed to the published version of the manuscript.

Funding: The study is partly funded by the Federal Ministry of Education and Research (BMBF) via ERUM-Pro and the EU project Radiate. In addition, the equipment used in this study from the FLAB-3Dprint research project is funded by dtec.bw—Forschungszentrum Digitalisierung und Technik der Bundeswehr, for which we would like to express our sincere thanks. dtec.bw is funded by the European Union—NextGenerationEU.

Data Availability Statement: The data presented in this study are available on request from the corresponding author.

Conflicts of Interest: Author Luis Catarino was employed by the company FKM Sintertechnik GmbH. Author Michael Doppler Catarino was employed by the company RENA Technologies Austria GmbH, Sa. The authors declare that the research was conducted in the absence of any commercial or financial relationships that could be construed as a potential conflict of interest. The companies FKM Sintertechnik GmbH and RENA Technologies Austria GmbH had no role in the design of the study; in the collection, analyses, or interpretation of data; in the writing of the manuscript, or in the decision to publish the results.

References

1. Wangler, T.P. *RF Linear Accelerators*, 2nd ed.; John Wiley & Sons: Hoboken, NJ, USA, 2008; pp. 98–121.

2. Witman, S. Ten Things you Might Not Know about Particle Accelerators. Symmetry Magazine, Fermi National Accelerator Laboratory. 2014. Available online: <https://www.symmetrymagazine.org/article/april-2014/ten-things-you-might-not-know-about-particle-accelerators> (accessed on 1 December 2023).
3. Kutsaev, S.V. Advanced technologies for applied particle accelerators and examples of their use. *Tech. Phys.* **2021**, *66*, 161–195. [[CrossRef](#)]
4. Lung, H.; Cheng, Y.C.; Chang, Y.H.; Huang, H.W.; Yang, B.B.; Wang, C.-Y. Microbial decontamination of food by electron beam irradiation. *Trends Food Sci. Technol.* **2015**, *44*, 66–78. [[CrossRef](#)]
5. Do Huh, H.; Kim, S. History of radiation therapy technology. *Korean Soc. Med. Phys.* **2020**, *31*, 124–134.
6. Amaldi, H.; Braccini, S.; Puggioni, P. High frequency linacs for hadrontherapy. *Rev. Accel. Sci. Technol.* **2009**, *2*, 111–131. [[CrossRef](#)]
7. Wilson, I.H. Cavity construction techniques. *Cern Accel. Sch. Eng. Part. Accel.* **1991**, *2*, 92–103.
8. Nassiri, A.; Chase, B.; Craievich, P.; Fabris, A.; Frischholz, H.; Jacob, J.; Jensen, E.; Jensen, M.; Kustom, R.; Pasquinelli, R. History and technology developments of radio frequency (RF) systems for particle accelerators. *IEEE Trans. Nucl. Sci. Inst. Electr. Electron. Eng.* **2016**, *63*, 707–750. [[CrossRef](#)]
9. Ghodke, S.R.; Barnwal, R.; Mondal, J.; Dhavle, A.S.; Parashar, S.; Kumar, M.; Nayak, S.; Jayaprakash, D.; Sharma, V.; Acharya, S.; et al. Machining and brazing of accelerating RF cavity. In Proceedings of the 2014 International Symposium on Discharges and Electrical Insulation in Vacuum (ISDEIV), Mumbai, India, 28 September–3 October 2014; pp. 101–104.
10. Pagani, C.; Bellomo, G.; Pierini, P. A high current proton linac with 352 MHz SC cavities. *arXiv* **1996**, arXiv:acc-phys/9609004.
11. Mickat, S.; Barth, W.; Clemente, G.; Groening, L.; Schlitt, B.; Ratzinger, U. The Status of the High-Energy Linac Project at GSI. *GSI Sci. Rep.* **2014**, 306.
12. Brinkmann, R.; Andruszkow, J.; Agababyan, A.; Ageyev, A.; Andruszkow, J.; Antoine, C.; Aseev, V.; Aune, B.; Ayvazyan, V.; Baboi, N.; et al.; *TESLA Technical Design Report—PART II The Accelerator*; DESY: Hamburg, Germany, 2001. Available online: <https://tesla.desy.de/> (accessed on 1 December 2023).
13. Calignano, F.; Manfredi, D.; Ambrosio, E.P.; Biamino, S.; Lombardi, M.; Atzeni, E.; Salmi, A.; Minetola, P. Overview on Additive Manufacturing Technologies. *Inst. Electr. Electron. Eng. IEEE* **2017**, *105*, 101–104. [[CrossRef](#)]
14. Attaran, M. The rise of 3-D printing: The advantages of additive manufacturing over traditional manufacturing. *Bus. Horizons* **2017**, *60*, 677–688. [[CrossRef](#)]
15. Torims, T.; Cherif, A.; Delerue, N.; Pedretti, M.F.; Krogere, D.; Otto, T.; Pikurs, G.; Pozzi, M.; Tatkus, A. Evaluation of geometrical precision and surface roughness quality for the additively manufactured radio frequency quadrupole prototype. *J. Phys. Conf. Ser.* **2023**, *2420*, 012089. [[CrossRef](#)]
16. Torims, T.; Pikurs, G.; Gruber, S.; Vretenar, M.; Ratzkus, A.; Vedani, M.; Lopez, E.; Bruckner, F. First proof-of-concept prototype of an additive manufactured radio frequency quadrupole. *Instruments* **2021**, *5*, 35. [[CrossRef](#)]
17. Hähnel, H. Update on the first 3D printed IH-type linac structure—proof-of-concept for additive manufacturing of linac RF cavities. *Proc. LINAC 22* **2022**, *22*, 170–173.
18. Hähnel, H.; Ateş, A.; Dedić, B.; Ratzinger, U. Additive Manufacturing of an IH-Type Linac Structure from Stainless Steel and Pure Copper. *Instruments* **2023**, *7*, 22. [[CrossRef](#)]
19. Frigola, P.; Agustsson, R.B.; Faillace, L.; Murokh, A.Y.; Gianluigi, C.; William, A.C.; Pashupati, D.; Frank, M.; Robert, A.; Joshua, K.S.; et al. Advance additive manufacturing method for SRF cavities of various geometries. In Proceedings of the Thomas Jefferson National Accelerator Facility (TJNAF), Newport News, Whistler, BC, Canada, 13–18 September 2015.
20. Creedon, D.L.; Goryachev, M.; Kostylev, N.; Sercombe, T.B.; Tobar, M.E. A 3D printed superconducting aluminium microwave cavity. *Appl. Phys. Lett.* **2016**, *109*, 032601. [[CrossRef](#)]
21. Riensche, A.; Carriere, P.; Smoqi, Z.; Menendez, A.; Frigola, P.; Kutsaev, S.; Araujo, A.; Matavalam, N.G.; Rao, P. Application of hybrid laser powder bed fusion additive manufacturing to microwave radio frequency quarter wave cavity resonators. *Int. J. Adv. Manuf. Technol.* **2023**, *124*, 619–632. [[CrossRef](#)]
22. Mayerhofer, M.; Mitteneder, J.; Dollinger, G. A 3D printed pure copper drift tube linac prototype. *Rev. Sci. Instrum.* **2022**, *93*, 023304. [[CrossRef](#)] [[PubMed](#)]
23. Mayerhofer, M.; Mitteneder, J.; Wittig, C.; Prestes, I.; Jägler, E.; Dollinger, G. First High Quality Drift Tube Linac Cavity additively Manufactured from Pure Copper. In Proceedings of the 14th International Particle Accelerator Conference (IPAC23), Venicem, Italy, 7–12 May 2022; p. 43.
24. Tran, T.Q.; Chinnappan, A.; Lee, J.K.Y.; Loc, N.H.; Tran, L.T.; Want, G.; Kumar, V.V.; Jayathilaka, W.A.D.M.; Ji, D.; Doddamani, M.; et al. 3D printing of highly pure copper. *Metals* **2019**, *9*, 756. [[CrossRef](#)]
25. Gruber, S.; Stepien, L.; Lopez, E.; Brueckner, F.; Leyens, C. Physical and geometrical properties of additively manufactured pure copper samples using a green laser source. *Materials* **2021**, *14*, 3642. [[CrossRef](#)] [[PubMed](#)]
26. Mayerhofer, M.; Dollinger, G. Manufacturing method for radio-frequency cavity resonators and corresponding resonator. Patent No. EP3944725A1, 2020.
27. Mayerhofer, M.; Brenner, S.; Helm, R.; Gruber, S.; Lopez, E.; Stepien, L.; Gold, G.; Dollinger, G. Additive Manufacturing of Side Coupled Cavity Linac Structures from Pure Copper—A First Concept. *Instruments* **2023**, *7*, 56. [[CrossRef](#)]
28. Rena Technologies GmbH. Surface Treatment of 3D-Printed Metal Parts. 2023. Available online: <https://www.rena.com/en/technology/process-technology/hirtisation> (accessed on 1 December 2023).

29. Dassault Systèmes; CST Microwave Studio. 2023. Available online: <https://www.3ds.com/de/produkte-und-services/simulia/produkte/cst-studio-suite/> (accessed on 1 December 2023).
30. Menzel, M.T.; Stokes H.K. *Users Guide for the POISSON/SUPERFISH Group of Codes*; Technical Report; Los Alamos National Lab.: Los Alamos, NM, USA, 1987. [[CrossRef](#)]
31. Ronsivalle, C.; Picardi, L.; Ampollini, A.; Bazzano, G.; Marracino, F.; Nenzi, P.; Snels, C.; Surrenti, V.; Vadrucci, M.; Ambrosini, F. First acceleration of a proton beam in a Side Coupled Drift tube Linac. *Europhys. Lett.* **2015**, *111*, 14002. [[CrossRef](#)]
32. Degiovanni, A.; Stabile, P.; Ungaro, D. LIGHT: A linear accelerator for proton therapy. In Proceedings of the NAPAC2016, Chicago, IL, USA, 9–14 October 2016; p. 32.
33. Robinson, J.; Munagala, S.P.; Arjunan, A.; Simpson, N.; Jones, R.; Baroutaji, A.; Govindaraman, L.T.; Lyall, I. Electrical conductivity of additively manufactured copper and silver for electrical winding applications. *Materials* **2022**, *15*, 7563. [[CrossRef](#)] [[PubMed](#)]
34. EOS GmbH. EOS Copper CuCP. In *Material Datasheet*; Electro Optical Systems (EOS GmbH): Munich, Germany, 2023.
35. Verdú, A.S. High-Gradient Accelerating Structure Studies and Their Application in Hadrontherapy. Ph.D. Thesis, Universitat de Valencia, Valencia, Spain, 2013.
36. Gold, G. A Physical Surface Roughness Model and Its Applications. *IEEE Trans. Microw. Theory Tech. Inst. Electr. Electron. Eng. IEEE* **2017**, *65*, 3720–3732. [[CrossRef](#)]

Disclaimer/Publisher’s Note: The statements, opinions and data contained in all publications are solely those of the individual author(s) and contributor(s) and not of MDPI and/or the editor(s). MDPI and/or the editor(s) disclaim responsibility for any injury to people or property resulting from any ideas, methods, instructions or products referred to in the content.